Appl Phys B (2010) 100: 233–242
DOI 10.1007/s00340-009-3811-6

Applied Physics B
Lasers and Optics

Optical feedback cavity-enhanced absorption spectroscopy (OF-CEAS) in a ring cavity

D.J. Hamilton · M.G.D. Nix · S.G. Baran · G. Hancock · A.J. Orr-Ewing

Received: 17 August 2009 / Revised version: 21 October 2009 / Published online: 12 November 2009

Abstract Optical feedback cavity-enhanced absorption spectroscopy (OF-CEAS) has been demonstrated by coupling a distributed feedback diode laser to a ring cavity. Frequency-selected light decaying from the ring cavity is retro-reflected, inducing a counter-propagating intra-cavity beam, and providing optical feedback to the laser. At specific laser-to-cavity distances, all cavity mode frequencies return to the diode laser with the same phase, allowing spectra to be accumulated across the range of frequencies of the current-tuned laser. OF-CEAS has been used to measure very weak oxygen isotopologue ($^{16}O^{18}O$ and $^{16}O^{17}O$) absorptions in ambient air at wavelengths near 762 nm using the electric-dipole forbidden O_2 *A*-band. A bandwidth reduced minimum detectable absorption coefficient of 2.2×10^{-9} cm^{-1} Hz$^{-1/2}$ is demonstrated.

PACS 42.55.Px · 42.60.Da · 42.62.Fi

1 Introduction

Cavity ring-down spectroscopy (CRDS) and the related cavity-enhanced absorption spectroscopy (CEAS) are ultra-sensitive absorption spectroscopy techniques finding wide ranging applications as analytical tools. In the first demonstration of CRDS [1], a pulsed dye laser was used to excite an optical cavity and the subsequent rate of decay of light from the cavity analysed to obtain wavelength-dependent absorption losses. The optical path length enhancement of $(1 - R)^{-1}$ offered by this technique, where R is the cavity mirror intensity reflectivity, allows very weak absorptions to be measured. Since its initial application, numerous improvements and variations on the original technique have been made [2–8]. The coupling of an optical cavity to a continuous wave laser (CW-CRDS [9, 10]) permits a greater build up of light intensity inside the cavity than for pulsed laser CRDS. A fast optical switch then allows a ring-down to be observed. Increased signal intensity improves the spectrometer sensitivity while the reduction in laser bandwidth possible with CW lasers improves the spectral resolution of this technique. Further, active locking of the laser frequency to a resonant frequency of the cavity increases the injection efficiency, detection limit and data acquisition rate [11], but at the cost of greater experimental complexity. An alternative technique to CW-CRDS is CEAS [12, 13] in which absorptions are detected by instead measuring the total transmitted light intensity through the cavity at resonant mode frequencies. Thus the enhanced path length and high sensitivity of CRDS is preserved while the signal processing is simplified since neither fast transient data acquisition nor fitting of exponential decays are required. Comparative studies of CEAS and CRDS have shown that the former method is, in general, inherently less sensitive [14, 15], primarily due to the nature of the measurement because the cavity output intensity is subject to laser intensity fluctuations.

The development of tuneable, compact and relatively inexpensive continuous wave semiconductor lasers, driven by the telecoms industry, has fueled the design of CW CRD

D.J. Hamilton · M.G.D. Nix · A.J. Orr-Ewing (✉)
School of Chemistry, University of Bristol, Cantock's Close, Bristol BS8 1TS, UK
e-mail: a.orr-ewing@bris.ac.uk
Fax: +44-117-9250612

S.G. Baran · G. Hancock
Department of Chemistry, Physical and Theoretical Chemistry Laboratory, University of Oxford, South Parks Road, Oxford OX1 3QZ, UK

Present address:
M.G.D. Nix
School of Chemistry, University of Leeds, Leeds LS2 9JT, UK

spectrometers with the potential to perform *in field* measurements of key atmospheric species [16, 17]. Recently, the value of optical feedback (OF) locking of a diode laser to an optical cavity has been recognised. OF CRDS [18] is increasingly used because of benefits over standard CW-CRDS such as greater signal intensity and kilohertz acquisition rates [19]. In principle it offers a less expensive set-up because fast optical switches and high levels of optical isolation are not required. Greater sensitivity should also result from increased intra-cavity light intensity.

The effect of optical feedback on narrowing the bandwidth of semiconductor lasers is well understood [20, 21]. If a distributed feedback diode laser (DFB DL) is coupled to a high-finesse cavity and a fraction of the very narrow line width (∼10 kHz) intra-cavity radiation is allowed to return to the diode, it has the effect of seeding the laser, narrowing the laser bandwidth to below the line width of the cavity resonance and locking the laser to the frequency of the cavity mode. With the current applied to the laser continuously changing, however, after a time the locking range is exceeded and the laser can no longer operate at the cavity mode frequency. The laser frequency emitted must jump to either the frequency of a neighbouring mode or the free running condition, where the laser frequency scans continuously with applied current. OF-CRDS measurements are performed without a fast optical switch (such as an acousto-optic modulator, AOM) by chirping the laser with a square wave superimposed on the laser current. Throughout this ON pulse the laser scans, but the scan rate slows as equilibrium is reached. The laser locks to successive cavity modes for increasing periods of time, and towards the end of the current pulse, a steady state of cavity intensity is reached. The end of the ON pulse might be designed to extinguish the laser emission completely or to maintain emission but cause an abrupt change in the laser frequency, so that it detunes from the cavity mode. In either case, a cavity ring-down event can then be observed. Using this technique, detailed studies of absorption by trace gases [18] and extinction by aerosol particles have been undertaken [19, 22].

OF-CEAS also exploits the frequency narrowing and locking behaviour of semiconductor lasers to excite fully successive cavity modes, but instead of the square-wave ON pulse described above, involves a slow ramp of the laser frequency to monitor transmission at successive longitudinal modes. The resultant mode-by-mode CEAS method was first demonstrated by Morville et al. [23] using a V-shaped optical cavity. This technique is well suited to in situ studies of atmospheric constituents, being capable of measuring single or multiple absorption profiles during a single scan of the laser. Consequently, it has a growing range of applications, including in situ measurements of atmospheric methane [24], geothermal gases [25], water [26] and carbon dioxide isotopologues [27], and laboratory measurements of NO_2[28] and CO_2 isotopologues with applications in breath analysis [29].

Currently the most widely used optical feedback design for CRD/CEAS measurements is the V-cavity [18] created by folding a conventional linear cavity about its centre with the addition of a third mirror. This is a variation of the original tilted confocal cavity used to stabilise the frequency of a semiconductor laser [30]. Creating a cavity with three mirrors means the geometry is such that the angle of incidence of the input laser beam on the central folding mirror is not normal, so most of the radiation incident on the cavity input mirror is reflected away from the laser beam path and does not return to the laser. Only a small subset of the frequencies within the laser bandwidth is resonant with cavity modes and can couple into the cavity. The frequency selected light ringing down from inside the cavity can, however, feed back to the laser, narrowing the output bandwidth and increasing the efficiency of injection of light into the cavity. In the current work, possible advantages are explored of the use of a triangular ring cavity rather than a V-shaped folded linear cavity.

Our ring cavity is illustrated in Fig. 1 and also uses three mirrors to ensure, by geometry, that the reflection of the incident laser beam directly from the cavity input mirror does not return to the laser. Once light of the resonant frequency enters the cavity, it propagates as a travelling wave around the cavity. Ring cavity resonant frequencies (ω_n) correspond to a phase change of 2π after a single round-trip of length L_R. Angular frequencies ($\omega = 2\pi c/\lambda$ for a wavelength λ) resonant within the cavity are given by (1), where

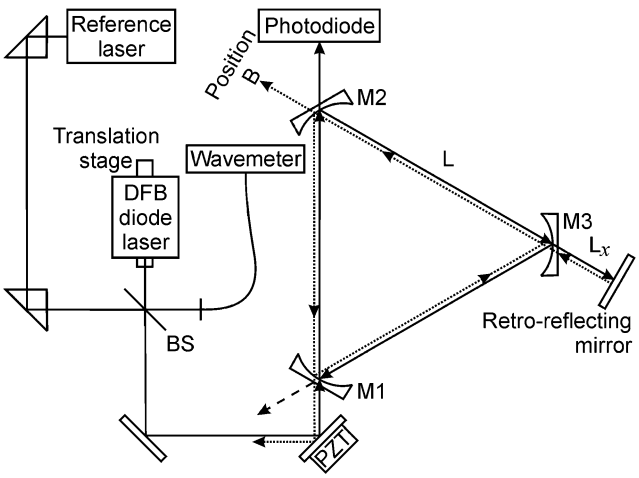

Fig. 1 Ring cavity set-up. The *solid arrows* depict the propagation of the main laser beam in the cavity. The *dotted arrows* depict the propagation of the retro-reflected beam. Abbreviations used: BS = beam splitter; M1, M2, M3 = first, second, third cavity mirror; L = path length between reflections; L_x = path length between third cavity mirror (M3) and retro-reflecting mirror; PZT = piezoelectric transducer. Note that the wavemeter is fibre coupled. Position B is used as a photodiode location to monitor the standing wave generated in the cavity by the retro-reflecting external mirror

n is any integer and c is the speed of light in the intra-cavity medium.

$$\omega_n = \frac{2n\pi c}{L_R} \quad (1)$$

To allow optical feedback to occur, a mirror is placed after either the second (M2) or third (M3) cavity mirror to retro-reflect escaping light back into the cavity so that it can propagate along the TEM_{00} cavity mode in the opposite direction. When this counter-propagating light exits from the cavity through the first input mirror (M1) it follows the cavity input path back to the laser diode where it can lock the laser's emitted frequency to that of the excited cavity mode. Without the retro-reflecting mirror in place, an additional source of optical feedback is seen, causing an erratic enhancement of random cavity modes. This feedback is caused by backscatter from the reflective surfaces of any of the three mirrors, returning light to the laser by exciting the counter-propagating TEM_{00} cavity mode. With careful cleaning of the cavity mirrors this backscatter is, however, insignificant relative to the light introduced into the counter-propagating TEM_{00} cavity mode by the retro-reflecting mirror.

Potential advantages of a ring cavity over a folded linear cavity may now be identified. First, the ring cavity does not display odd and even modes associated with standing waves present in a folded linear cavity [23]. Second, the retro-reflecting mirror allows the level of optical feedback experienced by the laser to be increased from near zero, without introducing attenuating optical elements between the laser and the cavity; such elements have the undesirable effect of reducing the power incident on the cavity input mirror (M1) and transmitted to the detector.

The absorption lines measured during this study to test the performance of OF-CEAS in a ring cavity lie in the atmospheric oxygen A-Band, corresponding to the $b^1\Sigma_g^+ \leftarrow X^3\Sigma_g^-(0,0)$ transition. This transition is very weak, being electric dipole (because of the g $\leftarrow \times \rightarrow$ g selection rule), spin (singlet $\leftarrow \times \rightarrow$ triplet) and symmetry ($\Sigma^+ \leftarrow \times \rightarrow \Sigma^-$) forbidden and is driven by a magnetic dipole interaction. The A-band was studied in detail by Dicke and Babcock [31], and later by Babcock and Herzberg [32]; these investigations determined molecular constants for $^{16}O^{16}O$ as well as for its two main rare isotopologues, $^{16}O^{18}O$ and $^{16}O^{17}O$. The most recent, high-accuracy studies were those undertaken by Robichaud et al. [33–36] using CRDS. $^{16}O^{16}O$ is a symmetric molecule containing two identical spin-0 nuclei, and thus in the ground state only odd N'' rotational angular momentum quantum states can be populated [37]. For $^{16}O^{16}O$ only half of the expected rotational lines therefore appear in the absorption spectrum. Lines arising from the less abundant isotopologues appear as weak features between the $^{16}O^{16}O$ absorption features: here, the $^{R}R(2)$ and $^{R}Q(1)$ lines of the $^{16}O^{18}O$ and $^{16}O^{17}O$ isotopologues (respective relative abundances of 0.00399 and 0.00074) are observed on the wings of much stronger $^{16}O^{16}O$ (relative abundance 0.99526) rotational lines [38] in ambient air samples. The oxygen A-band is of considerable importance in atmospheric science: the region from 755–770 nm contains very little absorption from other species, and the A-band is therefore used to retrieve vertical pressure and temperature profiles and to measure cloud top heights and pressures, as useful aids to weather prediction.

2 Experimental details

The ring cavity, shown in Fig. 1, consists of three high-reflectivity dielectric mirrors (Layertec) with radii of curvature of 1 m and a highly reflective region centred at 790 nm for 0° angle of incidence (AOI). In the configuration of an equilateral triangle, each cavity arm length is ~18.3 cm, and light is incident on each mirror at 30° AOI, shifting the highly reflective region by ~20 to ~770 nm. In our case of $R > 0.9999$ typical ring down times lie between 6 and 7 μs. To prevent the passage of dust through the intra-cavity beam the optical cavity and the retro-reflecting mirror are located inside a sealed chamber, containing ambient air at atmospheric pressure. The laser beam enters the chamber through wedged fused-silica windows.

A distributed feedback (DFB) diode laser (Sarnoff) emitting >10 mW of tunable 761 nm radiation is housed in a thermo-electrically cooled mount (Thorlabs), itself located on a translation stage (Thorlabs, 25 mm travel, micrometer precision). Temperature and current can be used to tune the emission frequency and are controlled by a Sacher Lasertechnik diode laser driver. When recording spectra, an asymmetric current ramp (20 Hz) is applied to the laser and the cavity output recorded for 1 s using a photodiode (New Focus, DC, 125 MHz) and a data acquisition card with a 14-bit vertical resolution (Gage CS1450). The resultant data file thus contains the result of 20 ramps of the laser.

The diode laser emission is steered by two silver mirrors and focussed into the centre of the first arm of the cavity by a single anti-reflection coated aspheric lens (numerical aperture 0.30), screwed directly into the laser mount. One of the silver mirrors is mounted on a PZT to adjust the laser to cavity distance with sub-wavelength precision. A thin glass plate between the laser and the first steering mirror serves to deflect a small portion of the beam into a wavemeter (Angstrom) and to introduce a visible reference beam, used for cavity alignment. All components are mounted on a vibration isolated optical table.

The emission from the diode laser is strongly polarised, and the DL mount is oriented so that vertically polarised light is emitted; this light is s-polarised relative to the optical cavity. Due to the non-normal angle of incidence upon

each cavity mirror this s-polarised light experiences a higher finesse than any p-polarised light circulating in the cavity. The s and p modes resonate in the ring cavity at different frequencies but with the same free spectral range [39]. At angles of incidence less than the Brewster's angle, p-polarised light (polarised in the ring plane) does not experience a π-phase shift upon reflection, whereas s-polarised light does (here, we adopt the conventions for phase and reference frame of [40] and neglect the effects of the multiple interface structure of dielectric mirrors). Thus, optical cavities with an odd number of mirrors will exhibit frequency splitting of the modes because of an accumulated phase shift difference of π, corresponding to a frequency difference of half a free spectral range. p-polarised light then resonates at frequencies shifted by half a free spectral range from modes of s-polarised light, as shown by Saraf et al. [39]. A polarising prism can be placed before the photodiode to select only the higher finesse s-polarised modes for analysis.

3 Theory

3.1 Molecular absorption from relative mode intensities

During the ramp of the applied laser current, if an excited cavity resonance lies at the frequency at which an intracavity gas absorbs, the beam intensity inside the cavity and so the detected intensity is reduced. From the measured cavity mode intensity and a measured or fitted background transmitted intensity, the absorption at discrete and well-defined cavity mode frequencies can be determined. From an analysis of the superposition of the amplitudes of the fields transmitted by the ring cavity, we obtain an expression for the cavity transfer function, the ratio of transmitted to incident light intensities (I and I_{in}, respectively), at the maxima of cavity modes for the ring-cavity configuration shown in Fig. 1:

$$\frac{I}{I_{\text{in}}} = \frac{T^2 e^{-\alpha L}}{(1 - R^{3/2} e^{-3\alpha L/2})^2} \tag{2}$$

Here, α is the intra-cavity absorption coefficient at the cavity mode frequency, and the three cavity mirrors are equidistantly separated by a distance L (so the cavity round-trip distance $L_R = 3L$).

In the experimental measurements described here, weak absorption spectra are obtained superimposed on an underlying absorption corresponding to the wings of much stronger spectral lines. As is described later, the background absorption losses are determined by measuring the transmitted baseline intensity (I_b) at selected mode frequencies and interpolating using a baseline fitting procedure. At a cavity mode frequency ω_n lying within the lineshape of the weak absorption feature of interest, the molecular absorption coefficient $\alpha_m(\omega_n)$ above the baseline level $\alpha_b(\omega_n)$ (such that the total absorption coefficient $\alpha = \alpha_m + \alpha_b$) is then obtained from a ratio of the interpolated baseline intensity to the transmitted value (I_b/I):

$$\alpha_m(\omega_n) = -\frac{1}{c\tau_b(\omega_n)} - \frac{2}{3L} \ln\left\{1 - \sqrt{\frac{I_b(\omega_n)}{I(\omega_n)}}\left(1 - e^{-3L/2c\tau_b(\omega_n)}\right)\right\} \tag{3}$$

In (3), $\tau_b(\omega_n)$ is the ring-down time corresponding to the baseline absorption losses $\alpha_b(\omega_n)$ at the frequency of the measurement. By taking the ratio of intensities in (3), the need to monitor the incident light intensity (2) is circumvented. The term $3L/2c\tau_b$ is much smaller than unity, allowing the simplification of (3) to the form:

$$\alpha_m(\omega_n) = \frac{1}{c\tau_b(\omega_n)}\left\{\sqrt{\frac{I_b(\omega_n)}{I(\omega_n)}} - 1\right\} \tag{4}$$

The spectral resolution of the mode-by-mode CEAS technique is limited by the free spectral range of the optical cavity.

3.2 Optical feedback phase and the laser-to-cavity distance

For reasons discussed in detail by Laurent et al. [20] and Morville et al. [23], the performance of an OF-CEAS spectrometer is optimized if the relative phase ϕ of the feedback light reaching the laser after returning from the cavity lies within a small range of values about $\phi = 0$. With an arbitrary laser to cavity distance, it is unlikely that light of different modal frequencies, corresponding to different values of n in (1), will have the same phase after propagation from the cavity back to the laser. The subtly different wavelength for each cavity mode gives a different number of field oscillations between two arbitrary points. It is therefore necessary to find a distance from the cavity to the laser where all feedback light has identical phase. The analysis must consider the source of optical feedback, i.e. the retro-reflecting mirror in our ring-cavity design, and the frequency of the feedback light itself. By following the analysis of the phase of optical feedback from a tilted confocal cavity [20] and a V-cavity [23] and applying the method to our ring cavity, we obtain that the path from the laser, through the cavity, and to the retro-reflecting mirror must equal a half integer number of cavity round-trip lengths, as shown in (5).

$$L_{L\to C} + NL + L_x = k\frac{L_R}{2} \tag{5}$$

Here $L_{L\to C}$ is the distance between the laser and the input cavity mirror (M1), L_x is the distance between the retro-reflecting mirror and the cavity and NL is the path length

through the cavity between the laser input mirror and the exit mirror behind which is located the retro-reflecting mirror. N can take the value 1 or 2 depending on whether the retro-reflecting mirror is positioned after the first or the second cavity mirror. For example, Fig. 1 shows the $N = 2$ configuration. L_R is the optical cavity round-trip distance and k is any integer. Under this condition all cavity mode frequencies undergo a phase change of 2π during their return trip to the laser and can lock the laser with maximum efficiency.

The condition expressed by (5) allows both L_x and $L_{L\rightarrow C}$ to be optimised. Weakly divergent light exiting from the cavity towards the retro-reflecting mirror is best returned after a short distance to maximise injection into the counter-propagating TEM_{00} mode. A planar silver mirror is sufficient for the retro-reflection. The laser to cavity distance can then take values separated by half the cavity round-trip distance. These are chosen to optimise the mode matching of the laser beam into the TEM_{00} cavity mode by matching the beam diameter on the cavity input mirror and the position of the intra-cavity beam waist. A ring cavity consisting of three identical spherically curved mirrors has a beam waist positioned at the centre of each cavity arm, but because of the non-normal incidence on the mirrors, each beam waist has an elliptical cross section [41].

The laser to cavity distance can be positioned correctly to within 5 μm by examining the effect of the variation of the phase of optical feedback across ∼175 cavity modes, corresponding to a frequency range of ∼3.2 cm^{-1} ($\Delta\nu_{FSR} = 0.01824$ cm^{-1}). All modes in the scan then have peaks of excitation intensity within the cavity mode-locked range and mode-by-mode CEAS can be performed. Successful coupling of the optical feedback requires all mode frequencies returning from the cavity to interfere constructively with the emitted light, thus a node in the beam field must be present at the laser. Thermal drift and vibrations alter the laser to cavity distance, moving the node from the laser diode. Continuous readjustment of the laser to cavity distance is therefore necessary, and a feedback loop similar to those described in [42, 48] was implemented which differentiates each cavity mode, obtains an error signal proportional to the phase error by integrating the result and moves the laser beam steering mirror mounted on a PZT to adjust the laser to cavity distance. This feedback operation was performed using a LabVIEW program instead of electronic hardware and successfully corrects thermal drift of the laser to cavity distance, thereby allowing averaging of the cavity output signal over many successive scans of the laser frequency.

3.3 Modelled and measured counter-propagating mode intensities

The generation of the counter-propagating beam allows optical feedback to occur, locking the laser to excited cavity mode frequencies. However, the level of feedback experienced by the laser at each locked frequency is not uniform.

As the laser scans in wavelength across a cavity mode, light of the resonant frequency enters the optical cavity and propagates around the ring, decaying from each mirror. Of the light reflected by the external retro-reflecting mirror back towards the cavity, a small fraction ($\leq 1 - R$) incident on the cavity re-entry mirror (M3) can re-enter the cavity and couple back into the cavity in the opposite direction. The counter-propagating beam forms a weak standing wave by interference with a small proportion of the initial input beam circulating in the cavity. The standing wave field has a fixed node at its source, the retro-reflecting mirror, and extends into and around the ring cavity. Two points exist inside the cavity, at $L_R/2$ and L_R from the retro-reflecting mirror, where the standing waves for all mode frequencies have a node. The standing wave gives rise to a weak travelling component that decays from the cavity through mirror M1 and feeds back to the laser.

The rate of optical feedback is determined by the amplitude of the standing wave and is not equal for all cavity modes. When the laser is sited according to (5) every mode has identical phase after returning to the laser diode, but this in-phase condition is not met at the inner face of each cavity mirror. Consecutive cavity modes have an additional phase change of 2π, adding two nodes to the standing wave component of the intra-cavity light field. The different field amplitude at each cavity mirror means that different reflectivities are experienced by each cavity mode, with angular frequency ω_n. The magnitude of the standing wave on each cavity mirror can be modelled, an estimated reflectivity applied for each mirror and a cavity mode intensity calculated from the average reflectivity. This process gives a pattern with a rough periodicity in the intensity of the counter-propagating beam. If a detector is sited at position B, see Fig. 1, the intensity of the counter-propagating beam can be measured and similarities are observed in the simulated pattern, as shown in Fig. 2.

It should be noted that the mode-to-mode intensity variation is of the standing wave in the cavity and of the resultant travelling component escaping from the cavity and providing feedback. The travelling wave used for detection of molecular absorptions by CRDS/CEAS experiences *the same* mode-to-mode reflectivity independent of frequency. The variation of the rate of optical feedback on these modes used for CEAS is, however, seen as a slight mode-to-mode intensity variation during CEAS measurements. This effect could therefore limit the minimum detectable absorption coefficient achievable through CEAS with a ring shaped cavity.

The relative intensity of the counter-propagating beam in the cavity, induced by the retro-reflecting mirror, relative to the forward-propagating beam can be as much as ∼0.03, as measured by comparison of both cavity outputs. If allowed

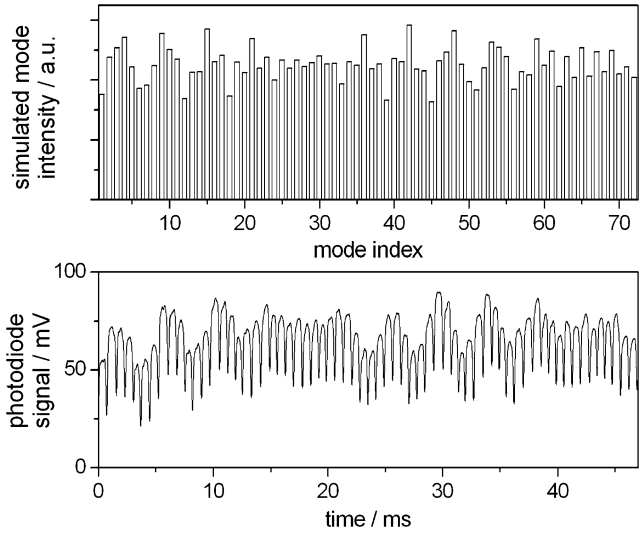

Fig. 2 *Upper panel*: simulated counter-propagating cavity mode intensities incorporating the different possible field amplitudes of the intra-cavity standing wave on each cavity mirror. The cavity arm lengths, L, used are accurate to 10^{-3} m, when compared to the experimental apparatus, but 10^{-9} m precision is required for an exact model. *Lower panel*: measured counter-propagating mode structure at position B. A periodicity similar to that calculated in Fig. 2 is seen despite use of approximate cavity arm lengths in the simulation

to return to the laser, this level of feedback causes mode hopping, and sequential cavity modes are not reliably excited during a mode-by-mode OF-CEAS scan, most notably during the high-current regime towards the end of the rising current ramp. It is therefore necessary to reduce the intensity of the counter-propagating beam so that the rate of optical feedback is sufficient for the laser to lock to each cavity mode, for just less than the time taken by the laser to scan through a single free spectral range. This can be achieved by adjusting a variable neutral density filter located between the optical cavity output mirror (M3) and the retro-reflecting mirror. An alternative method is to misalign slightly in the vertical direction the reflection from the retro-reflecting mirror. Due to the significant horizontal ellipticity of the laser output, horizontal misalignment of the retro-reflecting mirror has the undesirable tendency to excite (and thus cause the laser to lock to) higher order modes in the ring plane, such as TEM_{10} and TEM_{20} modes. Neither of these techniques requires any form of optical attenuator between the laser and the cavity, such as a polarising prism, which would reduce the power incident on the optical cavity.

The ring cavity, together with other optical feedback designs, maintains an ease of switching from CEAS to CRDS measurements. No hardware modifications are necessary; instead the triangular wave superimposed on the applied laser current is switched to a square wave and the OF phase locking software maintaining the laser to cavity distance is configured to differentiate only the first few cavity modes excited. The final mode, over which the laser locks for an extended period of time, shows little phase information on its top; instead the mode intensity is dominated by amplitude fluctuations of the laser emission, so this mode is ignored in the phase locking program. An advantage of using the ring cavity to perform OF-CEAS/CRDS is the absence of odd and even modes, found when using a V-cavity design [23]. The terms odd and even describe the alternating reflectivity experienced by consecutive cavity modes due to the phase of the standing wave inside the cavity at the folding cavity mirror. The different reflectivities cause alternate cavity modes to experience alternating intensity build-ups and ring-down times. This effect can be corrected during the data analysis stage by treating sets of data points arising from alternate modes separately, and combining the two sets of results once transformed to absolute absorption units. Alternatively the laser to cavity distance can be adjusted so that only odd or even modes are in phase upon returning to the laser and can feed back. While this latter methods simplifies the data collection, it increases the mode spacing to twice the free spectral range of the cavity, halving the spectral resolution. This reduced resolution may be offset by creating a longer optical cavity because $\Delta\nu_{FSR} \propto L^{-1}$.

For completeness we note that other techniques exist that have demonstrated OF-CRD/CEAS measurements. These include the use of a Brewster-angle optic within the cavity [42] and a technique exploiting the residual birefringence of cavity mirror coatings [43]. OF-CRDS with a linear cavity has also been attempted in our laboratory using a pinhole between the diode laser and the optical cavity to spatially filter the frequency selected intra-cavity beam decaying from the cavity from the direct reflection from the cavity input mirror [44]. After extensive modelling of relative beam paths between the laser and the cavity and application of possible optical designs, no sufficiently robust solution to this latter strategy was found. Using a ring shaped cavity Zare and workers have also employed OF cavity-enhanced spectroscopy methods to measure Rayleigh scattering cross sections; D.S. Kuramoto, R.N. Zare, Private communication (2009).

4 Detection of weak absorptions

With a high finesse optical cavity, R values typically greater than 0.9999 (corresponding to a minimum finesse of 31400, $\tau_0 \approx 6.5$ µs) and optical feedback, very weak absorptions can be measured for gaseous samples. Here we illustrate the performance of mode-by-mode OF-CEAS in the ring cavity using three absorption lines in the oxygen A-band in air under ambient conditions. A simulation of all oxygen absorptions present in the frequency range of the diode laser (~761–762 nm) is shown in Fig. 3. The enlargement of the region centred at 13130 cm^{-1} lies between two well

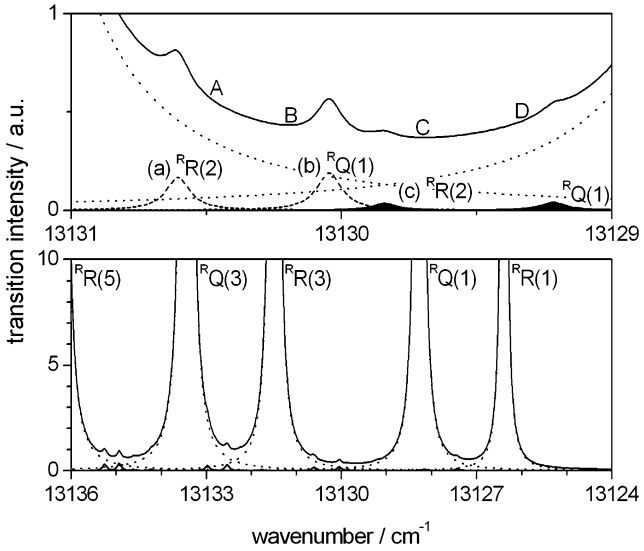

Fig. 3 HITRAN 2008 simulation of the absorptions due to molecular oxygen ($P = 1$ atm, $T = 22$°C) [38]. Rotational line assignments are given in the form ${}^{\Delta N}\Delta$J(N″). *Lower panel*: from 13136 to 13124 cm^{-1}. Note the very weak absorption lines of ^{16}O^{17}O and ^{16}O^{18}O. The *solid line* is the composite of absorption by the three isotopologues considered here. *Upper panel*: enlargement centred on the region recorded using OF-CEAS. Lines marked (a), (b) and (c) were measured, see Table 1. The *upper solid curve* is the composite spectrum comprising ^{16}O^{16}O (*dotted*), ^{16}O^{18}O (*dashed*) and ^{16}O^{17}O (*filled*). Frequencies marked A to D are used to obtain the background ring-down time, τ_b, as detailed in the text

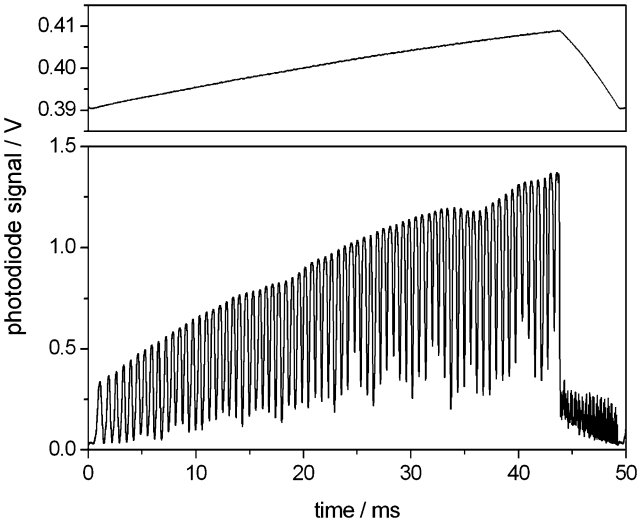

Fig. 4 *Lower panel*: mode-by-mode OF-CEAS cavity output signal showing two weak absorptions by ^{16}O^{18}O (lines (a) and (b) in Table 1), at 18 and 36 ms. The current ramp applied during the scan causes an increase in the emitted laser power (shown in the *upper panel*) and a corresponding increase in cavity mode intensity, seen as a general rising trend in the *lower panel*

Table 1 Transition frequencies of four isotopologue absorptions between 13131 and 13129 cm^{-1}, the isotopic abundance and rotational line assignment [38]. Absorption lines labelled (a), (b) and (c) were measured in air under ambient conditions

Isotopologue	Abundance	Rotational line assignment, ${}^{\Delta N}\Delta J(N'')$	Transition frequency/cm^{-1}
^{16}O^{18}O	0.399%	RR(2)	13130.605 (a)
		RQ(1)	13130.045 (b)
^{16}O^{17}O	0.074%	RR(2)	13129.839 (c)
		RQ(1)	13129.217

separated ^{16}O^{16}O lines and contains four isotopologue absorptions, with details provided in Table 1. The relatively strong ^{16}O^{16}O absorptions lie sufficiently close together that their wings overlap and significant molecular absorption is present at all frequencies. The simulation shown in Fig. 3 does not consider the underlying continuum in this band due to collision-induced absorption (CIA) [45].

A ramp of the applied current over 65 modes ($\sim$1.2 cm^{-1}) at 20 Hz allows the laser to lock to each mode for $\sim$0.7 ms, sufficient time to allow complete excitation. An asymmetric ramp for the applied laser current improves the effective work cycle by using a shorter interval to return the current to its initial value. Excitation of the cavity modes occurs during the slower rising ramp of the pulse, which occupies a longer period of time than the down ramp. Figure 4 shows the mean cavity output signal after one second of averaging at a laser scan rate of 20 Hz. The ^{16}O^{18}O isotopologue absorptions (a) and (b) (see Table 1) at ambient temperature, pressure and concentration in air are seen as dips in the transmitted intensity through the cavity.

The cavity output signal is recorded for 1 s and the resultant data file contains the result of 20 ramps of the laser. Individual spectra are analysed using a peak detection algorithm (LabVIEW) based on a quadratic least squares fit and the maximum intensity of each mode obtained. The mean intensity, $I(\omega_n)$, and standard deviation, SD$[I(\omega_n)]$, of each mode at its discrete resonant frequency is determined. An analytically fitted polynomial baseline provides the background cavity mode intensities, $I_b(\omega_n)$. This baseline is chosen to exclude rare isotopologue absorptions although it includes any CIA and ^{16}O^{16}O absorptions as required by (3) or (4). The background ring-down time, τ_b, used for absolute calibration is also inclusive of cavity losses caused by CIA and the wings of ^{16}O^{16}O absorption lines, but exclusive of isotopologue absorptions, which is achieved by taking ring-down measurements at mode positions marked A, B, C and D in Fig. 3. A polynomial fit through these four points was used to determine the background ring-down time of all modes excited by the laser scan. This method thus includes cavity losses due to mirror transmission and all underlying absorption. The resultant absorption spectrum containing lines (b) and (c) is shown in Fig. 5 as a function of the mode index (a running number which is incremented by the free spectral range of the cavity). A spectrum of the ^{16}O^{18}O RR(2) line (a) is presented in Fig. 6.

Table 2 Comparison of measured integrated line intensities (σ_{INT}) and collisional-broadened half widths (γ_{air}) of three oxygen isotopologue lines with the values given in the HITRAN database.[38] Standard errors are given by the uncertainty in the fit and displayed in parentheses in units of the least significant digit

		OF-CEAS	HITRAN	OF-CEAS	HITRAN
		$\sigma_{INT}/10^{-27}$ cm^2 molec.$^{-1}$ cm^{-1}		γ_{air}/cm^{-1} atm^{-1}	
(a)	$^{16}O^{18}O$ $^{R}R(2)$	4.79(14)	5.73	0.0438(17)	0.0546
(b)	$^{16}O^{18}O$ $^{R}Q(1)$	5.68(25)	6.73	0.0469(23)	0.0564
(c)	$^{16}O^{17}O$ $^{R}R(2)$	1.02(17)	1.18	0.0411(74)	0.0546

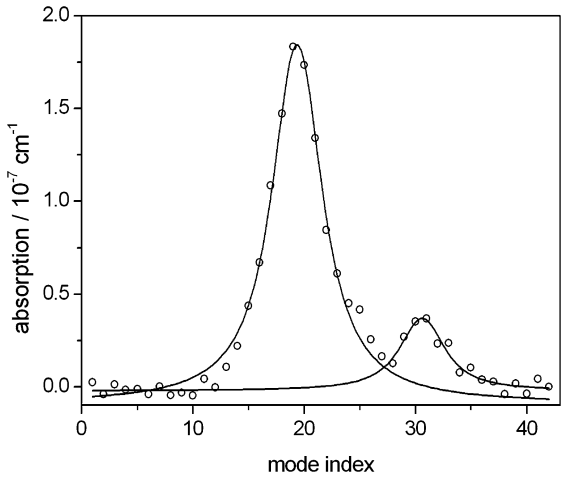

Fig. 5 Absorption spectrum of two weak oxygen lines in the $b^1\Sigma_g^+ \leftarrow X^3\Sigma_g^-(0,0)$ transition measured under ambient conditions. The stronger is the $^{R}Q(1)$ line of $^{16}O^{18}O$ at 13130.045 cm^{-1}. The weaker absorption is the $^{R}R(2)$ line of $^{16}O^{17}O$, at 13129.839 cm^{-1}. *Circles* indicate absorptions determined from cavity modes; the *solid lines* are Voigt profile fits

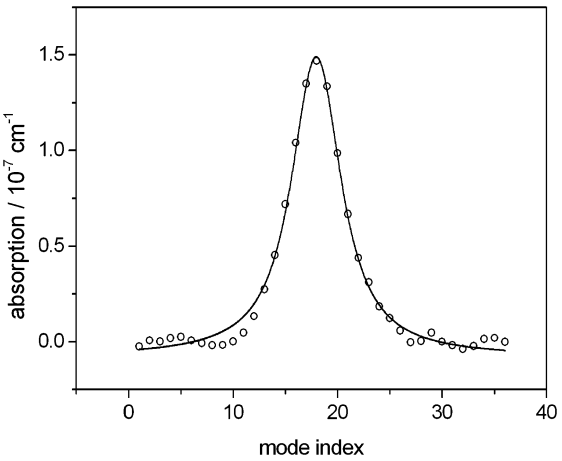

Fig. 6 Absorption spectrum of the $^{R}R(2)$ line of $^{16}O^{18}O$ at 13130.605 cm^{-1} in the $b^1\Sigma_g^+ \leftarrow X^3\Sigma_g^-(0,0)$ transition measured under ambient conditions. The experimental measurements (*circles*) obtained in 1 s are fitted to a Voigt profile (*solid line*)

A Voigt profile is fitted to each measured absorption line by floating all parameters except the Doppler (Gaussian) contribution to the width, which is fixed at the expected value for the temperature of the gas. The total area of the absorption multiplied by the free spectral range of the cavity, i.e. the mode separation, gives an integrated absorption coefficient, α_{INT} (cm^{-2}). This can be analysed using (6) to obtain the integrated line intensity, σ_{INT} (cm^2 molec.$^{-1}$ cm^{-1}):

$$\alpha_{INT} = \sigma_{INT}[O_2] \tag{6}$$

$[O_2]$ is the concentration of oxygen in the laboratory and is dependent on the ambient air pressure and temperature. An air pressure of 1000 mbar at 22°C corresponds to a concentration of oxygen in the air of 5.14×10^{18} molec. cm^{-3}. Pressure fluctuations of ±2% are possible as a result of changing weather conditions, corresponding to a probable molecular number density of between 5.03×10^{18} molec. cm^{-3} and 5.24×10^{18} molec. cm^{-3}. The spectrum was taken during a period of good settled weather in which the Bristol air pressure was ∼1020 mbar and so the latter value was used for analysis. Table 2 shows the results for integrated line intensities and pressure broadened Lorentzian half widths obtained from the Voigt fits to the data in Figs. 5 and 6.

The collisionally broadened contribution to the line width is ∼three times greater than the Doppler contribution at ambient air pressure. As the entries in Table 2 demonstrate, the measured half widths of lines (a), (b) and (c) derived from the Lorentzian components of the Voigt fits are ∼15–25% lower than those given in the HITRAN database. The systematic uncertainties in our values will be fairly high, however, because of the signal-to-noise ratios for the very weak absorption lines, and the limited number of frequency points defining the lineshape. The combination of these factors restricted the lineshape analysis to fitting a Voigt function, when a more complicated lineshape function might be more appropriate. Differences also exist between the measured integrated line intensity and the literature values, with the measured values being 14–16% lower than those quoted in the HITRAN database. A number of factors may contribute to these differences: in particular, the removal of the complex underlying $^{16}O^{16}O$ absorption [45–47] using a polynomial fit to the baseline to extract the isotopologue absorption

may introduce an error in derived line intensities. The cavity mode powers were also not normalised with respect to the incident laser power; instead, any variation with diode laser current was accommodated in the baseline polynomial fit. The mode intensities and their corresponding ring-down times are not currently recorded simultaneously as in [48], and instead a time delay exists between the measurements. Larger discrepancies of up to ∼190% between measured and HITRAN data were observed by Motto-Ros et al. [48] while studying rare oxygen isotopologue lines in the O_2 B-band ($b \leftarrow X$, $1 \leftarrow 0$), using OF-CEAS with a linear cavity and Brewster-angle coupling method. In their case, the differences were attributed to difficulties in performing ab initio calculations of parameters for weak transitions for the entries in the HITRAN 2004 database. These calculations were made in 1998 [49] and have not been improved upon for the 2008 edition. The oxygen A-band literature values contained in HITRAN 2008 are the result of experimental studies, using isotopically enriched samples, and are therefore expected to be much more reliable [36]. These studies, mentioned in the Introduction, fitted the absorption profiles using Galatry line shapes to incorporate the effects of Dicke narrowing and line mixing.

We conclude that the small discrepancies between our line width and line intensity data and those in the current version of the HITRAN database are likely to arise from errors in our measurements resulting from the use of unenriched isotopologue samples, and the difficult calibration of background cavity losses (dominated by overlapping CIA features and the wings of the much stronger $^{16}O_2$ absorption lines). Nevertheless, the main purpose of the current work, to test the performance of a new design of OF-CEAS spectrometer, is successfully demonstrated and the instrument is shown to have sufficient sensitivity to observe $^{16}O^{18}O$ and $^{16}O^{17}O$ in ambient air in 1 s duration measurements via absorption on a weak, electric-dipole forbidden transition.

A common estimation of the sensitivity of any absorption technique is obtained from the minimum detectable absorption coefficient, $\alpha_{\min}$. For a single pass Beer-Lambert type absorption the minimum detectable absorption coefficient is largely dependent on the smallest detectable change in the beam intensity after passing through the sample. The sensitivity of CEAS is enhanced by the multi-pass effect of the high finesse cavity (by a factor of $(1 - R)^{-1}$, with $R = 0.999919$ as determined from $\tau_0 = 6.5$ µs for our apparatus), and (7) [6] provides a method to calculate $\alpha_{\min}$ values:

$$\alpha_{\min} = \frac{1}{c\tau_0}\frac{\Delta I_{\min}}{I_0} \tag{7}$$

I_0 is the mean output intensity, $\Delta I_{\min}$ is taken as $\sqrt{2}\mathrm{SD}[I(\omega_n)]$ and the minimum detectable absorption coefficient presented is the mean over all mode frequencies in the spectrum. Each spectrum is the mean result of several scans of the laser. 15 averages acquired in 0.5 s (laser scan rate: 30 Hz) yield a minimum detectable absorption coefficient of 1.2×10^{-8} cm^{-1}, corresponding to a bandwidth reduced sensitivity of $\alpha_{\min} = 2.2 \times 10^{-9}$ cm^{-1} Hz$^{-1/2}$. Consistent with this estimate, the residuals (experimental − fitted absorption) of the Voigt fit in Fig. 6 display a standard deviation of 3.9×10^{-9} cm^{-1} for a 1 s spectrum accumulation time. If a spectral line were to be measured against a background of zero absorption instead of the wings of $^{16}O^{16}O$ lines and the CIA, $\alpha_{\min}$ would be reduced to 2.0×10^{-9} cm^{-1} Hz$^{-1/2}$.

5 Conclusion

We have described the development and implementation of an OF-CEAS scheme using a ring-shaped cavity. A counter-propagating wave induced in the optical cavity by a retro-reflecting mirror provides optical feedback and forms a standing wave with a small proportion of the forward-propagating beam. The average field amplitude of the standing wave upon each mirror has been modelled and the expected mode structure compares well to the measured counter-propagating cavity output. The levels of feedback experienced at each cavity resonant frequency are not identical, and without careful mirror cleaning and fine control over the amount of re-injected counter-propagating light, relative mode amplitudes can be distorted by varying levels of feedback. The travelling wave that dominates the internal field in the ring cavity experiences the same reflectivity for each cavity resonant frequency and CRD measurements are therefore unaffected by the different feedback levels.

The required laser to cavity distance that allows all cavity mode frequencies to return to the laser with the same phase of optical feedback has been given. Fine adjustments of the laser to cavity distance necessary to correct for thermal drift and acoustic noise are controlled by analysing the shapes of the cavity modes in computer software and relaying a feedback signal to a piezo-electric optical mount.

Three weak absorptions in the oxygen A-band, caused by the rare isotopologues $^{16}O^{18}O$ and $^{16}O^{17}O$, at wavenumbers close to 13130 cm^{-1} have been measured in ambient air. The measured integrated line intensity and collisional-broadened half width of each absorption line were determined and compared to values reported in the HITRAN 2008 database. A bandwidth reduced minimum detectable absorption coefficient of 2.2×10^{-9} cm^{-1} Hz$^{-1/2}$ was achieved while measuring rare isotopologue absorptions superimposed upon a non-zero baseline of overlapping $^{16}O^{16}O$ absorption features and continuum CIA. With a non-absorbing background and mirrors of higher reflectivity the sensitivity of this technique could be further improved.

Acknowledgements Funding for this work, and for a studentship for DJH is gratefully acknowledged from EPSRC grant EP/E018297. SGB thanks the Analytical Trust Fund of the Royal Society of Chemistry for a studentship. AJOE thanks the Royal Society and Wolfson Foundation for a Research Merit Award.

References

1. A. O'Keefe, D.A. Deacon, Rev. Sci. Instrum. **59**, 2544 (1988)
2. J.J. Scherer, J.B. Paul, A. O'Keefe, R.J. Saykally, Chem. Rev. **97**, 25 (1997)
3. M.D. Wheeler, S.M. Newman, A.J. Orr-Ewing, M.N.R. Ashfold, J. Chem. Soc., Faraday Trans. **94**, 337 (1998)
4. G. Berden, R. Peeters, G. Meijer, Int. Rev. Phys. Chem. **19**, 565 (2000)
5. S.S. Brown, Chem. Rev. **103**, 5219 (2003)
6. M. Mazurenka, A.J. Orr-Ewing, R. Peverall, G.A.D. Ritchie, Annu. Rep. Prog. Chem., Sect. C **101**, 100 (2005)
7. C. Vallance, New J. Chem. **29**, 867 (2005)
8. G. Friedrichs, Z. Phys. Chem. **222**, 31 (2008)
9. D. Romanini, A.A. Kachanov, N. Sadeghi, F. Stoeckel, Chem. Phys. Lett. **264**, 316 (1997)
10. B.A. Paldus, J.S. Harris, J. Martin, J. Xie, R.N. Zare, J. Appl. Phys. **82**, 3199 (1997)
11. B.A. Paldus, C.C. Harb, T.G. Spence, B. Wilke, J. Xie, J.S. Harris, R.N. Zare, J. Appl. Phys. **83**, 3991 (1998)
12. R. Engeln, G. Beerden, R. Peeters, G. Meijer, Rev. Sci. Instrum. **69**, 3763 (1998)
13. A. O'Keefe, J.J. Scherer, J.B. Paul, Chem. Phys. Lett. **307**, 343 (1999)
14. M. Mürtz, B. Frech, W. Urban, Appl. Phys. B **68**, 243 (1999)
15. R. Peeters, G. Beerden, A. Ólafsson, L.J.J. Laafhoven, G. Meijer, Chem. Phys. Lett. **337**, 231 (2001)
16. W.R. Simpson, Rev. Sci. Instrum. **74**, 3442 (2003)
17. M. Pradhan, M.S.I. Aziz, R. Grilli, A.J. Orr-Ewing, Environ. Sci. Technol. **42**, 7354 (2008)
18. J. Morville, D. Romanini, A.A. Kachanov, M. Chenevier, Appl. Phys. B **78**, 465 (2004)
19. T.J.A. Butler, J.L. Miller, A.J. Orr-Ewing, J. Chem. Phys. **126**, 174302 (2007)
20. Ph. Laurent, A. Clairon, Ch. Breant, IEEE J. Quantum Electron. **25**, 1131 (1989)
21. C.E. Wieman, L. Hollberg, Rev. Sci. Instrum. **62**, 1 (1991)
22. T.J.A. Butler, D. Mellon, J. Kim, J. Litman, A.J. Orr-Ewing, J. Phys. Chem. A **113**, 3963 (2009)
23. J. Morville, S. Kassi, M. Chenevier, D. Romanini, Appl. Phys. B **80**, 1027 (2005)
24. D. Romanini, M. Chenevier, S. Kassi, M. Schmidt, C. Valant, M. Ramonet, J. Lopez, H.-J. Jost, Appl. Phys. B **83**, 659 (2006)
25. S. Kassi, M. Chenevier, L. Gianfrani, A. Salhi, Y. Rouillard, A. Ouvrard, D. Romanini, Opt. Express **14**, 11442 (2006)
26. E.R.T. Kerstel, R.Q. Iannone, M. Chenevier, S. Kassi, H.-J. Host, D. Romanini, Appl. Phys. B **85**, 397 (2006)
27. R. Wehr, S. Kassi, D. Romanini, L. Gianfrani, Appl. Phys. B **92**, 459 (2008)
28. I. Courtillot, J. Morville, V. Motto-Ros, D. Romanini, Appl. Phys. B **85**, 407 (2006)
29. S.G. Baran, G. Hancock, R. Peverall, G.A.D. Ritchie, N.J. van Leeuwen, Analyst **134**, 243 (2009)
30. B. Dahmani, L. Hollberg, R. Drullinger, Opt. Lett. **12**, 876 (1987)
31. G.H. Dicke, H.D. Babcock, Proc. Natl. Acad. Sci. USA **13**, 670 (1927)
32. H.D. Babcock, L. Herzberg, Astrophys. J. **108**, 167 (1948)
33. D.J. Robichaud, J.T. Hodges, P. Maslowski, L.Y. Yeung, M. Okumura, C.E. Miller, L.R. Brown, J. Mol. Spectrosc. **251**, 27 (2008)
34. D.J. Robichaud, J.T. Hodges, L.R. Brown, D. Lisak, P. Maslowski, L.Y. Yeung, M. Okumura, C.E. Miller, J. Mol. Spectrosc. **248**, 1 (2008)
35. D.J. Robichaud, J.T. Hodges, D. Lisak, C.E. Miller, M. Okumura, J. Quantum. Spectrosc. Radiat. Transfer **109**, 435 (2008)
36. D.J. Robichaud, L.Y. Yeung, D.A. Long, M. Okumura, D.K. Havey, J.T. Hodges, C.E. Miller, L.R. Brown, J. Phys. Chem. A (2009). doi:10.1021/jp901127h
37. W. Heisenberg, Z. Phys. **41**, 239 (1927)
38. L.S. Rothman, I.E. Gordon, A. Barbe, D.C. Benner, P.F. Bernath, M. Birk, V. Boudon, L.R. Brown, A. Campargue, J.-P. Champion, K. Chance, L.H. Coudert, V. Dana, V.M. Devi, S. Fally, J.-M. Flaud, R.R. Gamache, A. Goldman, D. Jacquemart, I. Kleiner, N. Lacome, W.J. Lafferty, J.-Y. Mandin, S.T. Massie, S.N. Mikhailenko, C.E. Miller, N. Moazzen-Ahmadi, O.V. Naumenko, A.V. Nikitin, J. Orphal, V.I. Perevalov, A. Perrin, A. Predoi-Cross, C.P. Rinsland, M. Rotger, M. Simeckova, M.A.H. Smith, K. Sung, S.A. Tashkun, J. Tennyson, R.A. Toth, A.C. Vandaele, J. Vander Auwera, J. Quantum. Spectrosc. Radiat. Transfer **110**, 533 (2009)
39. S. Saraf, R.L. Byer, P.J. King, Appl. Opt. **46**, 3850 (2007)
40. F.A. Jenkins, H.E. White, *Fundamentals of Optics* (McGraw-Hill, Singapore, 1981)
41. T. Skettrup, T. Meelby, K. Færch, S.L. Frederiksen, C. Pedersen, Appl. Opt. **39**, 4306 (2000)
42. V. Motto-Ros, J. Morville, P. Rairoux, Appl. Phys. B **87**, 531 (2007)
43. J. Morville, D. Romanini, Appl. Phys. B **74**, 495 (2002)
44. D.J. Hamilton, MSci Thesis. University of Bristol (2008)
45. G.D. Greenblatt, J.J. Orlando, J.B. Burkholder, A.R. Ravishankara, J. Geophys. Res. **95**, 18577 (1990)
46. K.M. Smith, D.A. Newnham, J. Geophys. Res. **105**, 7383 (2000)
47. H. Tran, J.-M. Hartmann, J. Geophys. Res. **113**, D18104 (2008)
48. V. Motto-Ros, M. Durand, J. Morville, Appl. Phys. B **91**, 203 (2008)
49. R.R. Gamache, A. Goldman, L.S. Rothman, J. Quantum. Spectrosc. Radiat. Transfer **59**, 495 (1998)